**Contract No.:**

This manuscript has been authored by Battelle Savannah River Alliance (BSRA), LLC under Contract No. 89303321CEM000080 with the U.S. Department of Energy (DOE) Office of Environmental Management (EM).

**Title page**

**Title:** Synthesis of CdZnTeSe single crystals for room temperature radiation detector fabrication: Mitigation of hole trapping effects using a convolutional neural network

**Author Information:**

1. Sandeep K. Chaudhuri, Ph.D., Department of Electrical Engineering, University of South Carolina, Columbia, SC 29208, USA. ORCID: 0000-0003-4277-121X
2. Joshua W. Kleppinger, B.S., Department of Electrical Engineering, University of South Carolina, Columbia, SC 29208, USA.
3. OmerFaruk Karadavut, M.S., Department of Electrical Engineering, University of South Carolina, Columbia, SC 29208, USA.
4. Ritwik Nag, B.S., Department of Electrical Engineering, University of South Carolina, Columbia, SC 29208, USA. ORCID: 0000-0003-0907-9950
5. Rojina Panta, M.S., Artificial Intelligence Institute, Department of Computer Science and Engineering, University of South Carolina, Columbia, SC 29208, USA.
6. Forest Agostinelli, Ph.D., Artificial Intelligence Institute, Department of Computer Science and Engineering, University of South Carolina, Columbia, SC 29208, USA. ORCID: 0000-0003-1392-3667
7. Amit Sheth, Ph.D., Artificial Intelligence Institute, Department of Computer Science and Engineering, University of South Carolina, Columbia, SC 29208, USA. ORCID: 0000-0002-0021-5293
8. Utpal N. Roy, Ph.D., Savannah River National Laboratory, Science, Engineering and Energy Directorate, Aiken, SC 29831, USA.
9. Ralph B. James, Ph.D., Savannah River National Laboratory, Science, Engineering and Energy Directorate, Aiken, SC 29831, USA. ORCID: 0000-0001-6573-2040
10. Krishna C. Mandal, Ph.D., Department of Electrical Engineering, University of South Carolina, Columbia, SC 29208, USA. ORCID: 0000-0002-7945-7366

**Corresponding author:** Krishna C. Mandal, Ph.D., Department of Electrical Engineering, University of South Carolina, Columbia, SC 29208, USA. ORCID: 0000-0002-7945-7366; e-mail: mandalk@cec.sc.edu

**Abstract:** In this article, we report the growth of $Cd_{0.9}Zn_{0.1}Te_{0.97}Se_{0.03}$ (CZTS) wide bandgap semiconductor single crystals for room-temperature gamma-ray detection using a modified vertical Bridgman method. Charge transport properties measured in the radiation detectors, fabricated from the grown CZTS crystals, indicated signs of hole trapping. Hole traps inhibit high-resolution radiation detection especially for energetic gamma-rays. Machine learning (ML) applications are gaining tremendous impetus in improving device and sensor performance by compensating for limitations arising from such intrinsic material properties. In this article, we describe a deep convolutional neural network (CNN) that has demonstrated remarkable efficiency in identifying the energy of a gamma photon detected by a CZTS detector. The CNN has been trained using simulated data that resemble output pulses from actual CZTS detectors when exposed to 662-keV gamma photons. The device properties required for the simulation have been derived from radiation detection measurements on a real $Cd_{0.9}Zn_{0.1}Te_{0.97}Se_{0.03}$ detector fabricated in our laboratory. The CNN has been trained with detector pulses arising through photoelectric (PE) and Compton scattering (CS) separately. The percentage error in predicting the detected energies, within an extremely small duration of 0.28 msec, were found to be lower than 0.1% for gamma energies higher than 50 keV for datasets containing PE and CS events

separately. The CNN has also been validated for a mixed PE and CS dataset to obtain a prediction error of 1%. The effect of detector resolution on the efficiency of the CNN has also been explored.

**Keywords:** CdZnTeSe (CZTS), crystal growth, vertical Bridgman method (VBM), room-temperature radiation detection, machine learning (ML), convolutional neural network (CNN).

**Acknowledgments:** Not appliable.

**Funding:** The authors acknowledge partial financial support provided by the DOE Office of Nuclear Energy's Nuclear Energy University Program (NEUP), Grant Nos. DE-AC07-051D14517 & DE-NE0008662. The work was also supported in part by the Advanced Support Program for Innovative Research Excellence-II (ASPIRE-II), #155300-21-57381 and ASPIRE-I (IIB), #155300-21-56895 of the University of South Carolina (UofSC), Columbia, USA, and Laboratory Directed Research and Development (LDRD) program within the Savannah River National Laboratory (SRNL).

**Conflicts of interest/Competing interests:** The authors have no conflicts of interest to declare that are relevant to the content of this article.

**Availability of data and material:** The data that support the findings of this study are available from the corresponding author upon reasonable request.

## 1. Introduction

Conventional high-resolution spectrometers for high energy x- and gamma-rays are based on lithium drifted silicon (SiLi) or high-purity germanium (HPGe) detectors. These detectors being made of narrow bandgap materials (Si:1.12 eV and Ge: 0.68 eV at 300 K) need to be cooled at cryogenic temperature for proper operation. The cryogenic attachments are generally bulky and needs constant monitoring, which limits the usage of these detectors as high energy x-/gamma-ray detectors in field applications such as homeland security, monitoring and safeguard of nuclear materials, and medical imaging. The semiconductor radiation detector community has since then worked to develop several wide bandgap compound semiconductors e.g., CdTe (1.5 eV), CdZnTe (1.6 eV), CdMgTe (1.56 eV), CdMnTe (1.72 eV), CdSe (1.70 eV), CdZnSe (2.0 eV), $HgI_2$ (2.15 eV), TlBr (2.68 eV), and $PbI_2$ (2.32 eV) in order to facilitate room-temperature detection of high energy gamma rays with unprecedented compact form-factor [1] - [3]. Apart from wide bandgap, the gamma-ray detector material should be composed of materials of high atomic number (high-Z) for efficient absorption of the energetic photons within a compact detector volume. For full energy deposition by the gamma photons into the detector, it is preferred that the gamma rays interact with the detector through the photoelectric effect, one of the three primary modes of interaction besides Compton scattering and pair production. Compton scattering is associated with partial energy deposition through inelastic scattering of gamma rays. Energy deposition through pair-production is unlikely for photon energies below 1.67 MeV and hence, will not be discussed in this article. The probability that a gamma photon of a particular energy interacts via photoelectric effect is proportional to $Z^{4-5}$, compared to Z and $Z^2$ for Compton scattering and pair production, respectively making high Z material suitable for efficient and high-resolution gamma ray detection [4].

Among the above-listed wide bandgap and high-Z compound semiconductors, CdZnTe (CZT) has by far been the most appropriate choice for radiation detection because of the additional characteristics such as high electrical resistivity and charge transport properties essential for high-resolution gamma detection [5] - [13]. High resistivity ensures low leakage current even for the high operating bias voltage required to establish the optimum electric field within the detector for efficient charge collection. Superior charge transport properties, such as high carrier mobility and lifetime, ensure high energy and timing resolution of semiconductor devices in general [14], [15]. High mobility and lifetime not only ensure complete and fast charge collection but also reflect that there are fewer charge trapping centers in the detector material which can affect the long duration and continuous operation of the detectors. Most of the prior-mentioned compound semiconductor detectors suffer from polarization effects, which limit their long-duration operation at a constant bias. Also, CZT fares better than the other materials when it comes to obtaining large volume crystals. However, low crystal growth yield (~33%) makes CZT production expensive as about only one-third (cumulative) of a grown ingot, is of detector grade. The presence of structural defects in CZT single crystals such as sub-grain boundary networks, twin/grain boundaries and cracks, mosaic structures, tilt boundaries, and dislocations prohibits obtaining large-volume detector grade CZT single crystals [6], [7], [16] - [17].

A recently discovered ternary compound semiconductor CdZnTeSe (CZTS) has demonstrated excellent gamma ray detection with energy resolution as high as that observed in CZT detectors and with a crystal growth yield of more than 90% [18] - [20]. The excellent crystal growth yield resulted due to the inclusion of Se in the CZT matrix, usually in 2-3 atomic percentage [21], [22], which reduces the concentration of sub-grain boundaries. High concentration of sub-grain boundary networks causes spatial charge transport inhomogeneity [18], [23]. CZTS ingots grown using both travelling heater method and horizontal Bridgman method have demonstrated excellent axial compositional homogeneity [18], [24] - [25]. With the combination of material properties similar to CZT and high crystal growth yield, CZTS is undoubtedly the future detector material for high resolution and economic medical imaging systems apart from other mainstream applications based on radiation detection [24], [26] - [29].

Despite the above-mentioned advantages, CZTS still suffers from poor hole transport properties, a limitation inherent to the presence of impurities in the precursor materials used for the crystal growth. While leaving the problem of producing high-purity precursor materials to the metallurgist, recently proven machine learning techniques can be adopted which predict the detected radiation energies with high accuracy using the existing detectors [30] - [36]. For instance, a major problem in multipixel or multi-detector arrays for positron emission tomography (PET) imaging is the false triggering of a pixel in a detector (intra-detector scatter) or a detector in an array (inter-detector scatter) by Compton scattered gamma rays [37]. Deep learning methods have been demonstrated to improve the sensitivity of such imaging systems [38]. In this article, we report the synthesis and growth of $Cd_{0.9}Zn_{0.1}Te_{0.97}Se_{0.03}$ high-resistivity single crystals using a vertical Bridgman method and use them to fabricate high energy gamma-photon detectors. We also demonstrate the effectiveness of a deep convolutional neural network (CNN) that can predict gamma energies with a high accuracy and within a fraction of a microsecond. The described CNN relies on pattern recognition in the raw detector pulses rather than in processed pulse shapes or pulse height spectra, which adds to the versatility and simplicity of trained gamma ray detection system.

## 2. Experimental Details

### *2.1. CdZnTeSe crystal growth*

Elemental precursors Cd, Zn, Te, and Se with 99.999% (5N) purity were further purified to obtain 7N purity using a multi-pass horizontal zone refining system [9]. The precursors were weighed to achieve the stoichiometric compound $Cd_{0.9}Z_{0.1}Te_{0.97}Se_{0.03}$ and sealed in a quartz ampoule under a high vacuum of $10^{-6}$ Torr. The sealed ampoule was placed in a three-zone Lindberg Blue furnace modified for vertical Bridgman growth. An axial temperature gradient of 3.5 ºC/cm was achieved by separately tuning the three heating zones. The quartz ampoule was tied to a quartz rod which was coupled to a DC motor for rotation. The slow rotation at 15 rpm ensures radial thermal uniformity. The entire ampoule-motor assembly was connected to a motorized frame which moved the rotating ampoule downward at a constant velocity of 3 mm/hour resulting in the directional solidification of the grown crystal. The motors for rotational and axial movements were computer controlled using an Arduino interface for precision control. Three axial passes were made to obtain the desired single crystalline purity following which the furnace was cooled down at progressively faster ramp rates starting with a slow rate to avoid any thermal stress. Once cooled, the quartz ampoule was taken out of the furnace and the ingot was extracted. The ingot was sliced into wafers which were used for detector fabrication. Fig. 1(a) and (b) shows the photographs of the grown CZTS ingot and a sliced wafer, respectively.

### *2.2 Detector fabrication*

Wafers were cut from the grown CZTS ingot and polished mechanically. The polishing procedure includes grinding using SiC paper down to 1500-grit size and lapping using alumina powder down to 0.05-µm grit size. The mechanically polished wafers were chemo-mechanically polished (CMP) using a 2% bromo-methanol solution for 1 min to obtain a mirror finish. The CMP also helps to reduce the effects of surface oxides. The dimensions of the CZTS wafer used for detector fabrication in the present study are $11.0\times11.0\times3.0$ $mm^3$. Gold contacts with similar dimensions were sputter coated on two opposite CMP polished surfaces to obtain planar detector geometry. The planar configuration, which ensures axially parallel and linear internal electric field, was used for the resistivity and the charge transport property measurements. The drift mobility value is needed for the simulation of detector pulses. Figure 2(a) and (b) shows the schematic diagram and a photograph of the CZTS detector, respectively used in this study.

*2.3 Radiation detection and data acquisition*

The CZTS detector was mounted on a custom-made printed circuit board (PCB) for securing electrical connections. The detector-PCB assembly was placed inside a metal test-box for minimizing external electromagnetic interference. The test-box was attached with coaxial connecters for biasing the detector and extraction of the detector signal. The test-box was also equipped with a vacuum port connected to a vacuum pump. It was continually evacuated during the alpha-ray measurements to minimize scattering of alpha particles by air molecules. The detector output signal was fed to a Amptek A250CF charge sensitive preamplifier, which produces voltage pulses proportional to the amount of energy deposited by the radiation incident on the detector. The preamplifier output pulses were fed to the data acquisition system for further processing. The data acquisition setup consisted of both conventional analog benchtop spectrometer and a custom-built digital pulse acquisition system. The conventional spectrometer comprises an Ortec 576 spectroscopy amplifier and a Canberra Multiport II multichannel analyzer (MCA). The MCA interface used a Genie 2000 software for data acquisition. The digital pulse recorder used a National Instrument PCI-5192 fast digitizer card. A LabVIEW interface for the digitizer card has been developed in-house to digitize and store preamplifier pulses. The schematic diagram of the data acquisition system is shown in Fig. 2(c).

*2.4 Data simulations*

Simulating data are an important part of training algorithms. In the present case a convolutional neural network needs to be trained for which large amounts of training data are required at several gamma photon energies. Obtaining detector pulses at different energies of gamma photons experimentally is often limited to the test gamma sources available. Detector output pulses with virtually any possible energy can be simulated and used for the training purpose provided they truly mimic the output of an actual preamplifier-detector assembly. In the present work a Monte-Carlo simulation was realized using a MATLAB code to generate radiation induced pulses. Detector pulses have been simulated for a CZTS detector exposed to the 662-keV gamma rays from a $^{137}$Cs radiation source. The parameters needed for pulse simulation such as electron-hole pair creation energy, material density, and gamma attenuation cross-sections have been obtained from standard literatures and toolkits such as NIST's XCOM web tool [1], [39], and material properties such as electron and hole mobilities have been calculated through experiments obtained on CZTS single crystals. A signal-to-noise ratio (*SNR*) of 20 has been added to the pulses of training data, which resulted in pulse height spectrum with peak FWHM resembling that of the real CZTS detector used in this study. More details on the pulse simulation have been published elsewhere [40]. The convolutional neural network described in this article was trained separately with detector signals arising from both photoelectric and Compton interactions. The photoelectric training data contain 10,000 detector pulses for a single photon energy. Each pulse is 10 μs long in duration. The sampling interval has been chosen to be $10^{-8}$ sec, a typical interval used in our digital spectrometer, which made the total number of data points corresponding to each energy equal to $10^7$. Such pulses were generated for each of the 70 different photon energies in the energy range 1 - 1000 keV. Compton pulses in similar numbers were simulated corresponding to each energy.

*2.5 Computational facilities*

The training and testing of the deep neural networks were carried out on Nvidia V100 graphical processing units (GPUs) at Artificial Intelligence Institute (AII) in collaboration with research center infrastructure of University of South Carolina (UofSC). The GPUs allow for the training of the CNN to be parallelized, which results in greatly reduced training times when compared to central processing units (CPUs).

## 3. $Cd_{0.9}Zn_{0.1}Te_{0.97}Se_{0.03}$ crystal characterization

A portion of the grown ingot from an area close to the location of the wafer taken for detector fabrication, was characterized using x-ray diffraction (XRD). The sharp diffraction peaks as seen in the

XRD scan in Fig. 3(a) suggest high-quality single crystalline nature of the grown ingot. The crystal planes corresponding to the peaks have been indexed using the peak positions present in the XRD scans of $Cd_{0.9}Zn_{0.1}Te$. Figure 3(b) shows an energy dispersive x-ray (EDX) spectrum recorded using a TESCAN Vega-3 SBU scanning electron microscope (SEM). The EDX spectrum showed the presence of all the precursors in atomic percentages close to the intended stoichiometry.

The charge transport properties define the performance of a radiation detector to a great extent. The drift mobility value defines how fast a charge carrier can transit under the influence of applied electric field. The drift mobility values are also needed to simulate the charge pulses used for training the CNN. The drift mobility for electrons and holes have been determined using a time-of-flight method [27]. In this method the preamplifier charge pulses obtained by exposing the detector to a $^{241}Am$ source are digitized and recorded. The rise-times of the pulses are measured using an algorithm coded in LabVIEW. Since alpha particles just penetrate the surface of the detector, the rise-time of a pulse depicts the transit time of the charge carriers. The transit time is the duration taken by a charge carrier to travel from the point of generation to its collection, which, for an axially linear and radially uniform electric field established within the crystal, correspond to the duration needed to traverse the thickness of the detector. The drift velocity can be calculated from the transit time for a given crystal thickness. The drift velocity is measured at different electric-field strength to obtain the drift mobility plot (drift velocity vs. electric field). The slope of the linear fit to the mobility plot gives the drift mobility. The polarity of the applied bias determines whether the electrons or holes traverse the detector thickness which in turn decides whether the mobility has been measured for the electrons or holes. The mobility plots obtained for both electrons and holes in $Cd_{0.9}Zn_{0.1}Te_{0.97}Se_{0.03}$ detector fabricated in the present work are shown in Fig. 4. The electron mobility was calculated to be 692 $cm^2/V/sec$ and 55 $cm^2/V/sec$ for electrons and holes, respectively. Similar difference in electron and hole drift mobilities in CZTS has been observed by others [41]. Drift mobility of holes, lower by an order of magnitude compared to that of electrons, suggests excessive hole recombination.

## 4. The CNN architecture

A neural network [42] is a class of non-linear function approximators made up of artificial neurons, also referred to as units, and artificial synapses or weights. Each weight is a scalar value that connects one neuron to another. During computation, each neuron outputs a numerical value that is determined by the value of its incoming connections, the value of the weights associated with each incoming connection, and an optional non-linear function. For example, in many applications of neural networks, the output of a neuron is a sigmoidal or rectified linear function of the weighted sum of input neurons to the neuron.

Training a neural network involves adjusting the values of the weights to improve the performance given by a user-specified function. Often, improvement in performance corresponds to reducing the value of a loss function. During training, the neural network is given example data as input, computes an output for this input data, and based on the output the neural network and the expected output, a loss is computed. The values of the weights are usually adjusted through a process called stochastic gradient descent [43].

Neural networks are often organized into groups of neurons called layers, where each layer is connected by a different set of weights. When data to be processed are structured, such as sound, in the one-dimensional case, or images, in the two-dimensional case, this structure can be exploited with convolutional neural network (CNN)s. CNNs offer several advantages over conventional machine learning classifiers. First and foremost, a CNN automatically learns and detects the important features in a dataset without any human supervision. Additionally, CNNs employ convolution, which amounts to weight sharing, where groups of neurons in a single layer are connected by the same set of weights. The weight sharing in CNN leads to significant reduction in complexity of the model and the number of weights. Each set of weights is typically referred to as a filter, and each intra-layer group of neurons is typically referred to as a channel. The stride of the convolution indicates how to increment the position of the weights. For example, a stride of one is a full convolution while a stride of two is a convolution that skips over one neuron each time. This will result in the subsequent layer having a dimensionality

that is half that of the original layer. The CNN architecture developed for this study is described in Fig. 5.

In this work, we train a CNN to identify the gamma photon energy of digital pulses obtained at the output of the preamplifier (see Fig. 2(c)). The input to the CNN contains $10^7$ points of raw measurement, which is equivalent to 100 msec of data. The CNN architecture has 7 one-dimensional convolutional layers with 50 channels each. Each convolutional filter is of size 11 where the first five layers have a stride of 2 and the last two layers have a stride of five. The 7 convolutional layers are followed by a fully connected layer of size 1000. The fully connected layer is followed by an output layer of size 1, which represents the estimation of the gamma photon energy. At all the layers except the output layer, the CNN uses rectified linear activation functions [44] and weight normalization [45]. Weight normalization removes the dependency on the magnitude of the weights when computing the output value of a neuron. The CNN was trained for 1 million iterations using the ADAM optimizer with a batch size of 100 [46]. The learning rate was initialized to 0.001 and is halved if the validation accuracy does not increase within 5000 iterations. The training set consisted of the first 90% of input data for each energy value, and the validation consisted of the remaining 10%.

## 5. Interaction of gamma photons with matter and charge trapping

In this section, the aspects of interaction of gamma photons with matter and the subsequent charge transport phenomena relevant for designing the CNN are reviewed. The way a gamma photon interacts with matter, a gamma ray of energy $E_\gamma$ can deposit its energy at any depth as far as it can penetrate within the detector material. While the probability of the photoelectric absorption is much higher at photon energies of a few eV to few hundred keV, the Compton scattering dominates between photon energies of a few tens of keV to few tens of MeV for most materials. In the present case of the detection of 662-keV gamma photons using CZTS detectors, the majority of the interactions are through Compton scattering. Multiple scattering leads to reduction in energy in thick detectors (in thin detectors the scattered gamma photon escapes leading to partial energy deposition), which eventually may lead to photoelectric absorption. The probability of photoelectric absorption $\sigma_{PE}$ per atom can be roughly expressed as [4]

$$\sigma_{PE} \cong \mathrm{k} \times \frac{Z^n}{E_\gamma^{3.5}} \quad \ldots (1)$$

where k is a constant and $n$ lies between 4 and 5. In summary, a gamma photon can interact through photoelectric absorption and produce a pulse depicting its full energy deposition or deposit partial energy through Compton scattering. For photon energies close to electron rest mass energy a gamma photon interacting through Compton scattering can deposit any energy between 0 to $\approx 2E_\gamma/3$ [4]. Hence, a CNN must be trained to distinguish between a detector pulse arising from a Compton scattering from a higher energy gamma photon or a photoelectric effect of lower energy gamma photons.

Additionally, the electronic pulse generated from a detector following a gamma photon interaction has noise embedded in it due to various statistical fluctuations such as scattering at the detector window, and fluctuations in the energy emitted by the radioactive source, energy deposited in the detector, number of charge pairs created, etc. The detector leakage current, detector capacitance, and electronic noise from the preamplifier add to the fluctuations of the output signal. These fluctuations increase the *SNR* in the output pulse. Hence, the CNN must be trained with data containing realistic *SNR*.

The above discussion does not take into consideration the fluctuations arising due to charge trapping within the detector material. Once the charge pairs are created from the photon-detector interaction, they start to drift under the influence of the applied electric field towards the electrodes with favorable polarity and are eventually collected to form the detector signal. In the presence of crystal defects, such as the hole traps in CZTS, electrons or holes are repeatedly trapped and detrapped by the defects before being collected. In the case of deep defects, the trapped charges often recombine and are permanently lost. While trapping-detrapping leads to the increment of rise-time of the charge pulses, recombination

leads to the reduction in pulse-height, both leading to fluctuation in the pulse shape. Figure 6 shows a biparametric correlation plot [5] obtained for the detector used in this study when exposed to 662-keV gamma photons emitted by a $^{137}$Cs radioisotope. The band of events due to the photoelectric (or full-energy deposition) events could be seen tilted towards the lower energy side for pulses with high rise-times, which is a result of the charge trapping in defects. Hence, the CNN must be trained with input data so as to learn the effect of charge trapping in the detector.

## 6. Results and discussions

### *6.1 Evaluation of the convolutional neural network*

Figures 7 (a) and (b) show the correlation of the energy predicted by the convolutional neural network ($E_{CNN}$) and the actual energy ($E_\gamma$) when trained and evaluated using the photoelectric and the Compton training datasets, respectively. The correlation plot in Fig. 7(a) shows a linear behavior for the case where the CNN has been trained using the photoelectric data. The linearity implies that any energy value in the range 1 - 1000 keV can be precisely made by the CNN. On the other hand, the correlation plot for the case of Compton data trained CNN (Fig. 7(b)) shows a linear behavior only for photon energies above 50 keV.

Figures 8 (a) and (b) show the variation of mean absolute error $\sigma$ in predicting the photon energy as a function of the actual energy when trained using the photoelectric and the Compton training datasets, respectively. The mean absolute error is defined as the absolute error $\left|E_{CNN} - E_\gamma\right|$ averaged over the predictions resulting from all the iterations. To distinguish between the training and evaluation of the CNN using photoelectric and Compton scattering datasets, the subscripts PE and CS will be used henceforth, respectively. The $\sigma_{PE}$ value is showed an increasing trend with increasing photon energies when the CNN has been trained and evaluated using the photoelectric event dataset. In contrast, for the case of the Compton event dataset, the $\sigma_{CS}$ values are found to be at least an order of magnitude higher than that seen in the case of the photoelectric events. Also, unlike $\sigma_{PE}$, any correlation of the variation of $\sigma_{CS}$ with $E_\gamma$ was not apparent. The overall larger $\sigma_{CS}$ values compared to $\sigma_{PE}$ are quite expected as the variation of pulse heights is extremely large in the case of single energy photon interacting through Compton scattering. As has been mentioned earlier, a gamma photon of energy $E_\gamma$ interacting through Compton scattering may partially deposit any energy in the range zero to $\approx 2E_\gamma/3$ for photon energies close to electron rest mass energy. The significance of increase in $\sigma_{PE}$ with $E_\gamma$ can be understood in the following way. In general, the signal-to-noise ratio of detectors is higher at higher incident energies as the number of generated charge carriers increase which improves the Fano factor. However, at higher energies the average penetration depth of the photons is higher which is why a greater number of holes take part in the charge transport. Charge transport properties corresponding to the holes are generally poor compared to that of the electrons in CZTS which leads to higher uncertainties in the pulse-heights and hence higher $\sigma_{PE}$ at higher energies. In the present CZTS detector the drift mobilities of electrons and holes have been calculated to be 692 and 55 cm$^2$/V/sec, respectively. These mobility values have been used for simulating the detector pulses. Moreover, in the present situation the effect of Fano statistics has not been considered while simulating the data. This variation is too subtle to be noticed in the case of variation of $\sigma_{CS}$ with photon energy where the error values itself are large.

For better representation the percentage error values, calculated as $\left(\sigma/E_\gamma\right) \times 100$, have been plotted in Figs. 9 (a) and (b) using the photoelectric and the Compton training datasets, respectively. The percentage errors have been observed to be higher at lower energies, however, the percentage error prediction was found to be pretty accurate for most energies with an error below 0.2% for photon energies above 20 keV. The maximum error was observed to be below 1% which was confined to energies below 20 keV. The percentage errors observed in the case of Compton dataset trained CNN were much higher at lower photon energies, however above 50 keV the percentage errors were seen to be much below 0.1%.

*6.2 Effect of signal-to-noise ratio on the performance of the CNN*

The preceding discussion has bypassed two fundamental aspects of radiation detection. First, the above-mentioned evaluation of the CNN uses separate data sets for photoelectric absorption and Compton events. In a practical situation, the detector would not *know* the type of interaction the gamma photon has undergone. Hence, we have simulated a data set containing detector pulses that originate from 662-keV photon-detector interactions only, and which contains both the photoelectric and Compton events. This type of dataset would be called *mixed* henceforth. Second, in a practical situation with multiple detectors in use, one cannot expect to have the same energy resolution (*SNR*) for every detector. The *SNR* determines the ultimate energy resolution of the detector as all the fluctuations involved in digital detection, and measurements are reflected as noise in the detector-preamplifier pulses. Normally, the higher the *SNR* is, the higher is the energy resolution. Hence, to investigate any correlation between the prediction accuracy of the CNN and detector resolution, we simulated data sets comprising detector pulses resembling the output of a CZTS detector exposed to 662-keV gamma rays for different *SNR* values between 5 - 100.

Figure 10 shows the variation of the percentage error in prediction when the mixed data set is evaluated with the Compton data trained CNN. The lowest prediction error of 1.2% was found to be around *SNR* = 10. The percentage error was seen to increase rapidly with higher *SNR* although the pulses are supposed to be more defined (cleaner) at higher *SNR*. It appears that the CNN does have a correlation with the *SNR*. Nonetheless, to understand any such correlation further studies are required by training the CNN with input data comprising of pulses of several *SNR*s. On the other hand, the percentage error obtained from the evaluation of the same dataset by the CNN trained by the photoelectric dataset resulted in error values close to 25%. It indicates that since the fraction of Compton events are naturally much more compared to that of the photoelectric events, the Compton trained CNN was more efficient in identifying the actual photon energy. At present we are trying to train the CNN with a mixed data set and varied *SNR*, and we anticipate that the error in prediction would be drastically minimized when it is validated on a mixed data set.

## 7. Conclusions

$Cd_{0.9}Zn_{0.1}Te_{0.97}Se_{0.03}$ single crystals have been synthesized using a vertical Bridgman method. The crystallinity and the stoichiometry have been confirmed using x-ray diffraction and energy dispersive x-ray scans. The drift mobility of holes was observed to be one order of magnitude lower than that of electrons. Poor drift mobility arises from excessive hole recombination leading to inaccurate energy detection in conventional pulse height spectroscopy. A deep convolutional neural network (CNN) has been designed to predict gamma ray energies based on pattern recognition of detector pulses instead of pulse height measurements. The CNN has been trained using a large dataset simulated to resemble pulses obtained at a CZTS detector output when exposed to gamma rays of various energies. Separate training dataset comprised of purely photoelectric (PE) or Compton scattering (CS) events were used for the training purpose. The gamma energy prediction capability of the CNN has been evaluated in terms of the percentage error of prediction. The CNN has been first validated separately for pure photoelectric data sets and Compton scattered data. Extremely low percentage errors (≤ 0.1%) have been obtained for both the cases for photon energies above 50 keV. When evaluated for a mixed dataset containing both PE and CS events, percentage errors close to 1% were observed. It has been observed that the CNN trained using the CS dataset performed better at least for photon energies above 50 keV, probably because of the larger number of events associated with the Compton scattering compared to that of the photoelectric events. It has also been observed that the efficiency of the CNN in predicting the photon energies accurately is much better for the *SNR* close to the one used to simulate the training data, 20 in the present case. The predictions did not improve for the detector pulses with higher *SNR*. It has been inferred that the efficiency of the CNN will be enhanced when it is trained simultaneously with both PE and CS data. Our future work also aims to evaluate the trained CNN for gamma photon energies obtained experimentally using several working detectors.

**Funding:** This work was supported by the DOE Office of Nuclear Energy's Nuclear Energy University Program (NEUP), Grant No. DE-AC07-051D14517 & DE-NE0008662. The work was also supported in part by the Advanced Support Program for Innovative Research Excellence-I (ASPIRE-I), Grant No. 15530- E404 and Support to Promote Advancement of Research and Creativity (SPARC), Grant No. 15530- E422 of the University of South Carolina (U*of*SC), Columbia, USA, and Laboratory Directed Research and Development (LDRD) program within the Savannah River National Laboratory (SRNL).

**Conflicts of interest/Competing interests:** The authors have no conflicts of interest to declare that are relevant to the content of this article.

## References

[1] A. Owens, A. Peacock, Nucl. Instrum. Meth. Phys. Res. A, **531**, 18 (2004).

[2] K. C. Mandal, S. H. Kang, M. Choi, A. Kargar, M. J. Harrison, D. S. McGregor, A. E. Bolotnikov, G. A. Carini, G. C. Camarda, R. B. James, IEEE Trans. Nucl. Sci., **54**, 802 (2007).

[3] S. K. Chaudhuri, R. M. Krishna, K. J. Zavalla, L. Matei, V. Buliga, M. Groza, A. Burger, K. C. Mandal, IEEE Trans. Nucl. Sci., **60**, 2853 (2013).

[4] G. F. Knoll, Radiation detection and measurements, (John Wiley, NJ, 2010).

[5] S. K. Chaudhuri, K. C. Mandal, in Advanced Materials for Radiation Detection, ed. By K. Iniweski (Springer Int., Cham, 2022), p. 211.

[6] T. E. Schlesinger, J. E. Toney, H. Yoon, E. Y. Lee, B. A. Brunett, L. Franks, R. B. James, Mater. Sci. Eng. R Rep., **32**, 103 (2001).

[7] S. Del Sordo, L. Abbene, E. Caroli, A. M. Mancini, A. Zappettini, P. Ubertini, Sensors*,* **9**, 3491 (2009).

[8] L. Abbene, G. Gerardi, F. Principato, A. Buttacavoli, S. Altieri, N. Protti, E. Tomarchio, S. Del Sordo, N. Auricchio, M. Bettelli, N. S. Amadè, S. Zanettini, A. Zappettini, J. Synchrotron Rad*.,* **27**, 1564 (2020).

[9] S. K. Chaudhuri, K. Nguyen, R.O. Pak, L. Matei, V. Buliga, M. Groza, A. Burger, K.C. Mandal, IEEE Trans. Nucl. Sci., **61**,793 (2014).

[10] M. Sajjad, S.K. Chaudhuri, J.W. Kleppinger, K.C. Mandal, IEEE Trans. Nucl. Sci., **67,** 1946 (2020).

[11] P. J. Sellin, A. W. Davies, S. Gkoumas, A. Lohstroh, M. E. Özsan, J. Parkin, V. Perumal, G. Prekas, M. Veale, Nucl. Instrum. Meth. Phys. Res. B, **266**, 1300-1306, (2008).

[12] K. A. L. Koch-Mehrin, S. L. Bugby, J. E. Lees, M. C. Veale, M. D. Wilson, Sensors, **21**, 3260 (2021).

[13] J. Zou, A. Fauler, A. S. Senchenkov, N. N. Kolesnikov, M. Fiederle, Crystals, **11**, 649 (2021).

[14] S. O. Kasap, M. Z. Kabir, K. O. Ramaswami, R. E. Johanson, R. J. Curry, J. Appl. Phys., **128**, 124501 (2020).

[15] M. Zahangir Kabir, E. V. Emelianova, V. I. Arkhipov, M. Yunus, S. O. Kasap, G. Adriaenssens, J. Appl. Phys., **99**, 124501 (2006).

[16] A. E. Bolotnikov, K. Ackley, G. S. Camarda, Y. Cui, J. F. Eγer, G. De Geronimo, C. Finfrock, J. Fried, A. Hossain, W. Lee, M. Prokesch, M. Petryk, J.L. Reiber, U. N. Roy, E. Vernon, G. Yang, R. B. James, IEEE Trans. Nucl. Sci., **62**, 3193 (2015).

[17] R. M. Krishna, S. K. Chaudhuri, K. J. Zavalla, K. C. Mandal, Nucl. Instrum. Meth. Phys. Res. A, **701**, 208, 2013.

[18] U. N. Roy, G. S. Camarda, Y. Cui, R. Gul, G. Yang, J. Zazvorka, V. Dedic, J. Franc, J. Franc, R .B. James, Sci. Rep., **9**, 7303, (2019).

[19] U. N. Roy, G. S. Camarda, Y. Cui, R. Gul, A. Hossain, G. Yang, J. Zazvorka, V. Dedic, J. Franc, R. B. James, Sci. Rep., **9**, 1620 (2019).

[20] S. K. Chaudhuri, J. W. Kleppinger, O. Karadavut, R. Nag, K. C. Mandal, Crystals, **11**, 827. (2021).

[21] U. N. Roy, G. S. Camarda, Y. Cui, R. B. James, Appl. Phys. Lett., **118**, 152101 (2021).

[22] S. K. Chaudhuri, M. Sajjad, J. W. Kleppinger, K. C. Mandal, IEEE Electron Dev. Lett., **41**, 1336 (2020).

[23] U. N. Roy, G. S. Camarda, Y. Cui, R. B. James, Appl. Phys. Lett., **114**, 232107 (2019)

[24] U. N. Roy, G. S. Camarda, Y. Cui, R. B. James, Radiation, **1**, 123 (2021).

[25] A. Yakimov, D. Smith, J. Choi, S. Araujo, Proc. SPIE, **1114**, 11141N (2019).

[26] R. Nag, S. K. Chaudhuri, J. W. Kleppinger, O. Karadavut, K. C. Mandal, J. Mater. Sci: Mater. Electron., **32**, 26740 (2021).

[27] S. K. Chaudhuri, M. Sajjad, J. W. Kleppinger, K. C. Mandal, J. Appl. Phys., **127**, 245706 (2020).

[28] S. K. Chaudhuri, M. Sajjad, K. C. Mandal, Appl. Phys. Lett., **116**, 162107 (2020).

[29] U. N. Roy, G. Camarda, Y. Cui, G. Yang, R. B. James, Sci. Rep., **11**, 10338 (2021).

[30] R.E. Abdel-Aal, M.N. Al-Haddad, Nucl. Instrum. Meth. Phys. Res. A, **391**, 275 (1997).

[31] V. Vigneron, J. Morel, M.C. Lepy, J.M. Martinez, Nucl. Instrum. Meth. Phys. Res. A, **369**, 642 (1996).

[32] W. P. Ford, E. Hague, T. McCullough, E. Moore, J. Turk, Proc. SPIE, **10644**, 106440G (2018).

[33] M. Kamuda, J. Zhao, K. Huff, Nucl. Instrum. Meth. Phys. Res. A, **954**, 161385 (2020).

[34] P. Zhou, S. Abbaszadeh, IEEE Nuclear Science Symposium and Medical Imaging Conference (NSS/MIC), (2020) https://doi.org/10.1109/NSS/MIC42677.2020.9507937.

[35] Z. Liu, S. Abbaszadeh, Sensors, **19**, 960 (2019).

[36] G. R. Romanchek, Z. Liu, S. Abbaszadeh, PLoS One, **15**, 0228048 (2020).

[37] Y. Gu, G. Pratx, F. W. Y. Lau, C. S. Levin, Med. Phys., **37**, 5494 (2010).

[38] N. Nasiri, S. Abbaszadeh, SPIE Proc., **11595**, 115953W (2021).

[39] XCOM NIST https://physics.nist.gov/PhysRefData/Xcom/html/xcom1.html. Accessed 12 Novemebr 2021.

[40] S. K. Chaudhuri, J. W. Kleppinger, R. Nag, K. Roy, R. Panta, F. Agostinelli, A. Sheth, U. N. Roy, R. B. James, K. C. Mandal, Proc. SPIE, **11838**, 1183806 (2021).

[41] J. Pipek, M. Betušiak, E. Belas, R. Grill, P. Praus, A. Musiienko, J. Pekarek, U. N. Roy, R. B. James, Phys. Rev. Appl., **15**, 054058 (2021).

[42] J. Schmidhuber, Neural Netw., **61**, 85 (2015).

[43] D. E. Rumelhart, J. L. McClelland, "Learning internal representations by error propagation," in [Parallel Distributed Processing: Explorations in the Microstructure of Cognition: Foundations], p. 318, (MIT Press, Cambridge, MA, 1987).

[44] K. Jarrett, K. Kavukcuogulo, M. Ranzato, Y. LeCun, in *2009 IEEE 12th International Conference on Computer Vision*, Kyoto, Japan, Oct. 2009, doi: https://doi.org/10.1109/ICCV.2009.5459469.

[45] T. Salimans, D. P. Kingma, Advances in Neural Information Processing Systems, **29**, 901 (2016).

[46] D. P. Kingma, J. Ba, Adam: A Method for Stochastic Optimization, arXiv:1412.6980v9 (2017) https://arxiv.org/abs/1412.6980.

## Figure captions:

**Figure 1**. A photograph of **(a)** the grown $Cd_{0.9}Zn_{0.1}Te_{0.97}Se_{0.03}$ ingot and **(b)** a wafer cut out from the ingot for detector fabrication.

**Figure 2**. **(a)** The schematics of a planar CZTS detector. **(b)** Photograph of a $Cd_{0.9}Zn_{0.1}Te_{0.97}Se_{0.03}$ detector used for radiation detection in the present work, and **(c)** The schematics for the gamma spectrometer used to capture digital pulses and analog pulse height spectra.

**Figure 3**. **(a)** Powder x-ray diffractogram of the grown $Cd_{0.9}Zn_{0.1}Te_{0.97}Se_{0.03}$ ingot **(b)** Energy dispersive x-ray spectrum obtained from the wafer processed for detector fabrication.

**Figure 4.** Variation of electron and hole drift velocity as a function of electric field strength in a $Cd_{0.9}Zn_{0.1}Te_{0.97}Se_{0.03}$ planar detector.

**Figure 5.** The architecture of the convolutional neural network used in the present work. Two of the seven one-dimensional convolutional layers have been shown. The rounded rectangular boxes represent the channels and the circles within represent the nodes.

**Figure 6.** A biparametric plot obtained from a $Cd_{0.9}Zn_{0.1}Te_{0.97}Se_{0.03}$ detector when exposed to 662-keV gamma photons emitted by a $^{137}Cs$ radiation source. The shaded region shows the overlapping of photoelectric and Compton events. The color bar on the top right side shows the intensity scale.

**Figure 7.** Correlation plots of the energies predicted for a given photon energy when the CNN has been trained with photoelectric events **(a)** and Compton events **(b)**.

**Figure 8.** Variation of mean absolute error in prediction of photon energies when the CNN has been trained with photoelectric events **(a)** and Compton events **(b)**.

**Figure 9.** Variation of the percentage error in prediction of photon energies when the CNN has been trained with photoelectric events **(a)** and Compton events **(b)**. The dotted lines mark the 0.1 percent error line.

**Figure 10.** Variation of percentage error in prediction of photon energies for different signal-to-noise ratio while the CNN has been trained for $SNR = 20$.

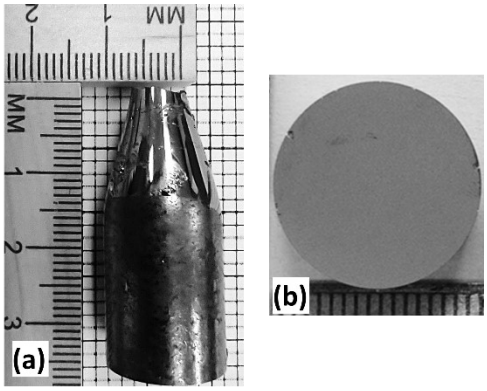


**Figure 1**. A photograph of **(a)** the grown $Cd_{0.9}Zn_{0.1}Te_{0.97}Se_{0.03}$ ingot and **(b)** a wafer cut out from the ingot for detector fabrication.

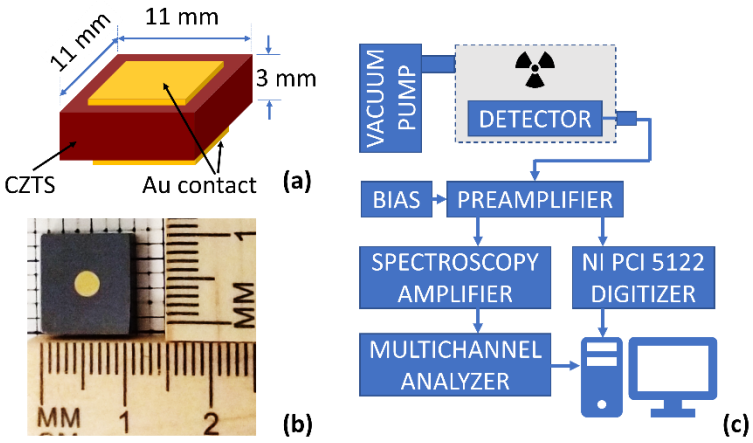


**Figure 2**. **(a)** The schematics of a planar CZTS detector. **(b)** Photograph of a $Cd_{0.9}Zn_{0.1}Te_{0.97}Se_{0.03}$ detector used for radiation detection in the present work, and **(c)** The schematics for the gamma spectrometer used to capture digital pulses and analog pulse height spectra.

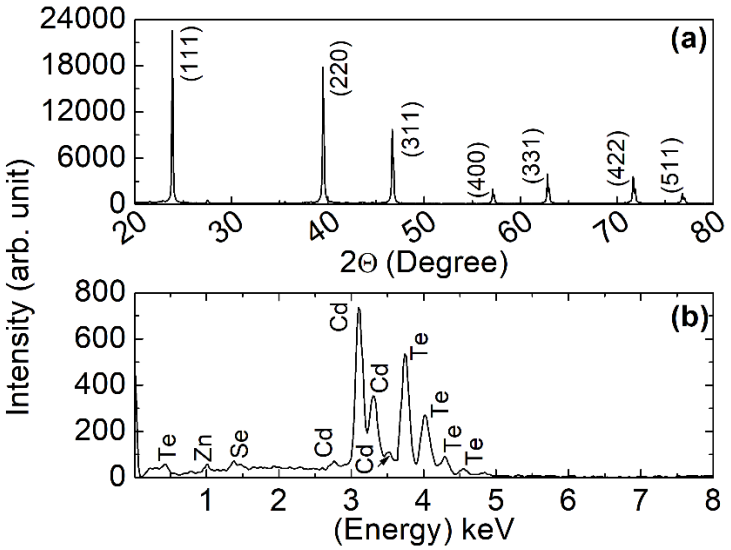


**Figure 3**. **(a)** Powder x-ray diffractogram of the grown $Cd_{0.9}Zn_{0.1}Te_{0.97}Se_{0.03}$ ingot, and **(b)** Energy dispersive x-ray spectrum obtained from the wafer processed for detector fabrication.

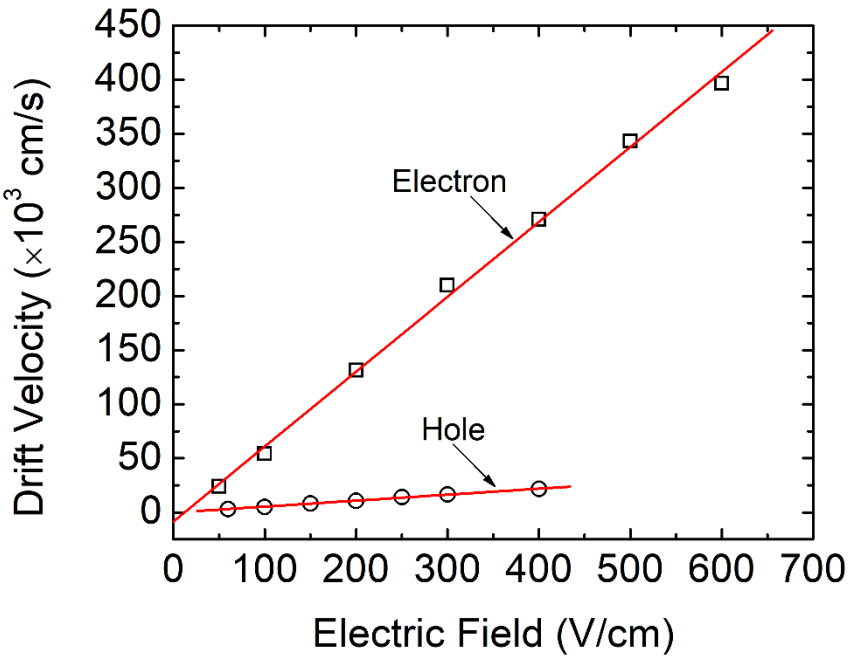


**Figure 4.** Variation of electron and hole drift velocity as a function of electric field strength in a $Cd_{0.9}Zn_{0.1}Te_{0.97}Se_{0.03}$ planar detector.

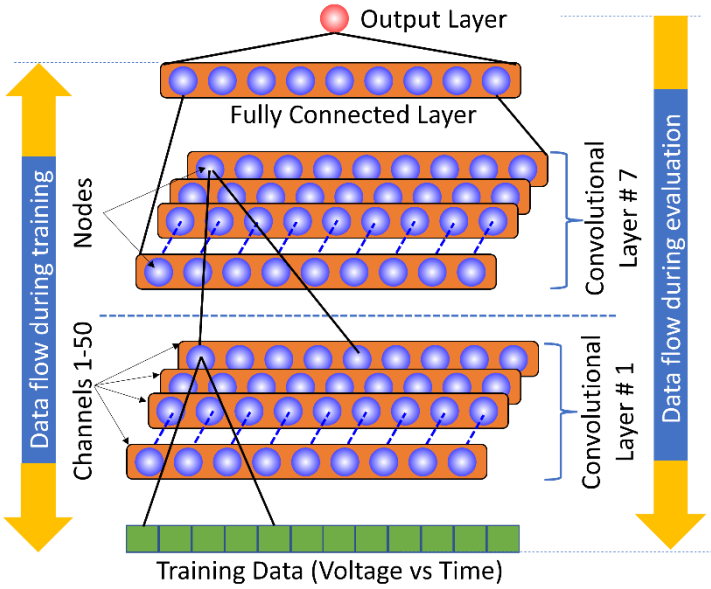


**Figure 5.** The architecture of the convolutional neural network used in the present work. Two of the seven one-dimensional convolutional layers have been shown. The rounded rectangular boxes represent the channels and the circles within represent the nodes.

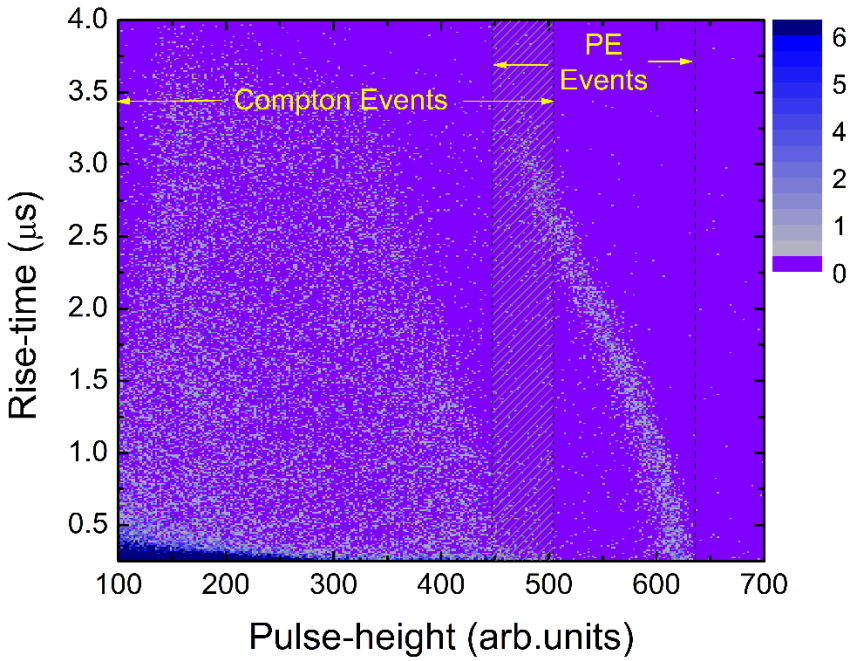


**Figure 6.** A biparametric plot obtained from a $Cd_{0.9}Zn_{0.1}Te_{0.97}Se_{0.03}$ detector when exposed to 662-keV gamma photons emitted by a $^{137}Cs$ radiation source. The shaded region shows the overlapping of photoelectric and Compton events. The color bar on the top right side shows the intensity scale.

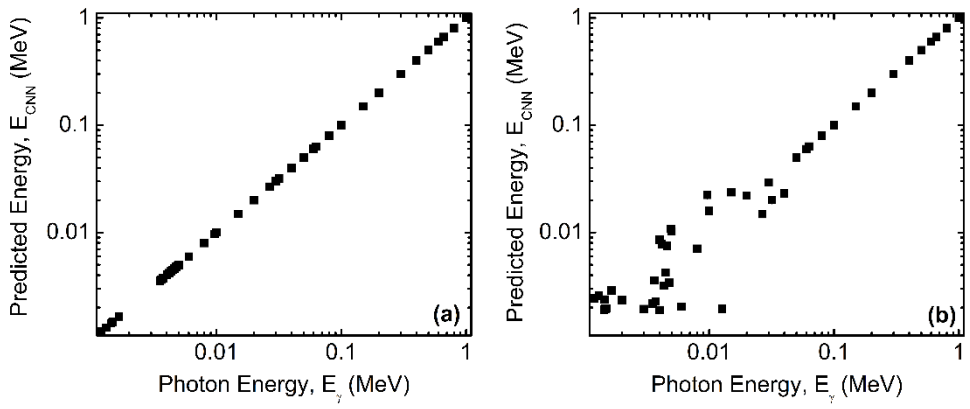


**Figure 7.** Correlation plots of the energies predicted for a given photon energy when the CNN has been trained with photoelectric **(a)** and Compton **(b)** events separately.

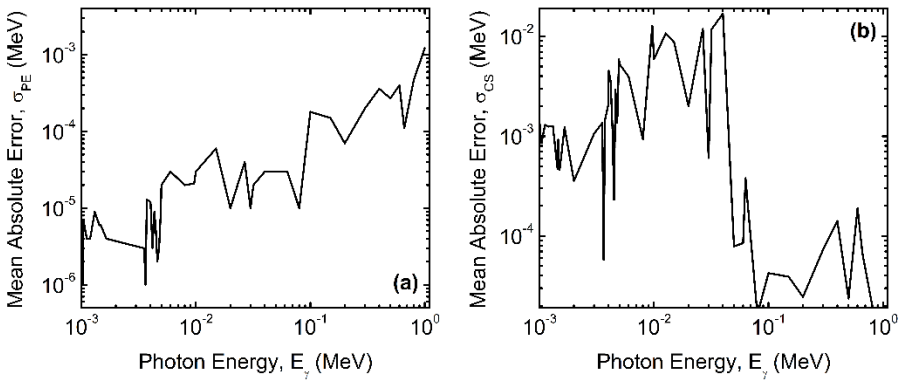


**Figure 8.** Variation of mean absolute error in prediction of photon energies when the CNN has been trained with photoelectric **(a)** and Compton **(b)** events separately.

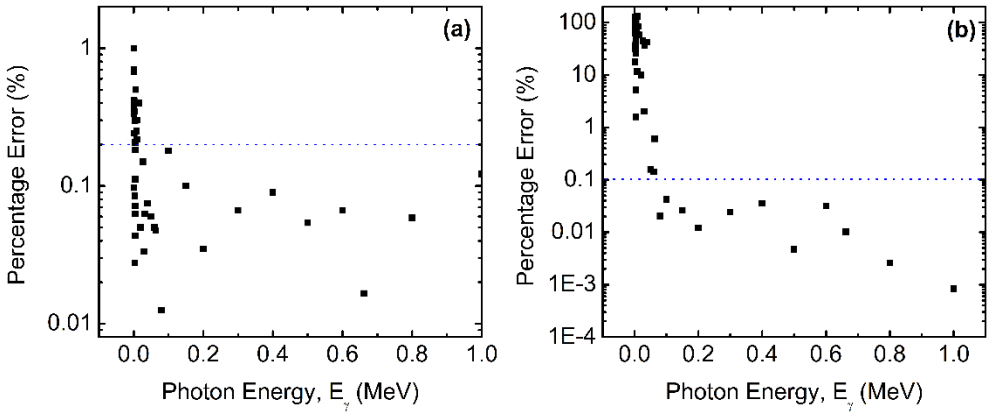


**Figure 9.** Variation of the percentage error in prediction of photon energies when the CNN has been trained with photoelectric **(a)** and Compton **(b)** events separately. The dotted lines mark the 0.1 percent error line.

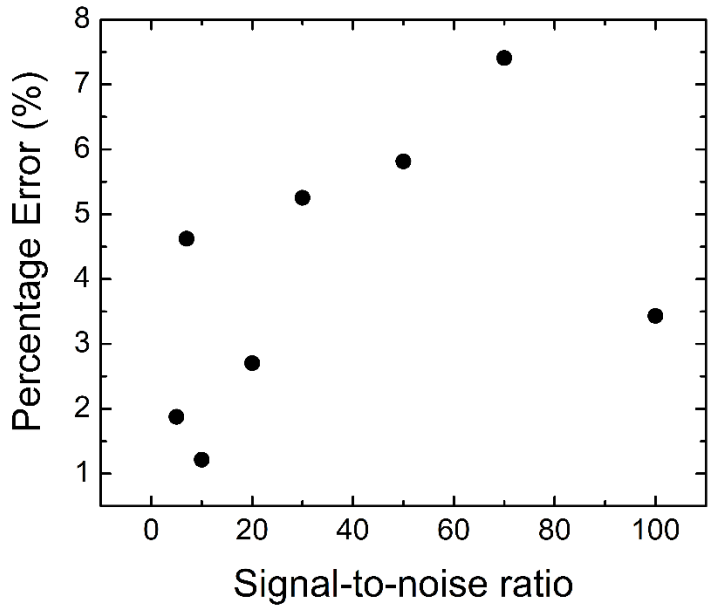


**Figure 10.** Variation of percentage error in prediction of photon energies for a mixed dataset for different signal-to-noise ratio while the CNN has been trained for *SNR* = 20.